ACS APPLIED MATERIALS & INTERFACES

Research Article

www.acsami.org

# Nanocasting Synthesis of $In_2O_3$ with Appropriate Mesostructured Ordering and Enhanced Gas-Sensing Property

Xiaohong Sun,*[,†] Haoran Hao,[†] Huiming Ji,[†] Xiaolei Li,[†] Shu Cai,[†] and Chunming Zheng*[,‡]

[†]School of Materials Science and Engineering, Key Lab of Advanced Ceramics and Machining Technology, Tianjin University, Tianjin 300072, P.R. China

[‡]State Key Laboratory of Hollow-fiber Membrane Materials and Membrane Processes, School of Environmental and Chemical Engineering, Tianjin Polytechnic University, Tianjin 300387, P.R. China

Supporting Information

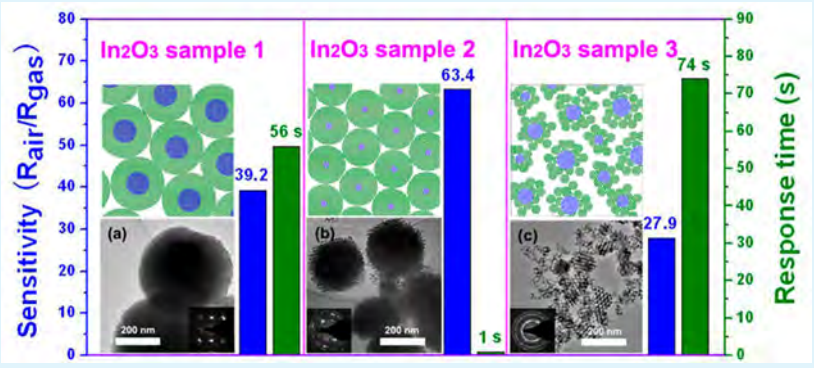


**ABSTRACT:** Ordered mesoporous $In_2O_3$ gas-sensing materials with controlled mesostructured morphology and high thermal stability have been successfully synthesized via a nanocasting method in conjunction with the container effect. The mesostructured ordering, as well as the particle size, crystallinity and pore size distribution have been proved to vary in a large range by using the XRD, SAXRD, SEM, TEM, and nitrogen physisorption techniques. The control of the mesostructured morphology was carried out by tuning the transportation rate of indium precursor in template channel resulting from the different escape rate of the decomposed byproducts via the varied container opening and shapes. The particular relation between the mesostructured ordering and gas sensing property of mesoporous $In_2O_3$ was examined in detail. It was found that the ordered mesoporous $In_2O_3$ with appropriate mesostructured morphology exhibited significantly improved ethanol sensitivity, response and selectivity performances in comparison with the other ordered mesoporous $In_2O_3$, which benefits from the large surface area with enough sensing active sites, proper pore distribution for sufficient gas diffusion, and appropriate particle size for effective electron depletion. The resulting sensing behaviors lead to a better understanding of designing and using such mesoporous metal oxides for a number of gas-sensing applications.

**KEYWORDS:** *$In_2O_3$, mesoporous structure, gas sensor, nanocasting synthesis, ethanol detection*

## INTRODUCTION

Nanostructured metal oxides, including 0D nanoparticles/nanospheres, 1D nanorods/nanotubes, 2D film/flake structures, and 3D porous/hollow structures, have been a hot topic in material science and engineering because of their superior function compared with their solid counterparts in a series of applications such as catalysis, energy storage, therapeutics and sensor.[1−5] The performance of nanostructured materials strongly depends on their morphology, structure, and material size.[6−9] Among them, nanostructured porous metal oxides have been reported to exhibit better gas-sensing, catalytic, or electrical properties than solid samples as the interconnected pores in the materials are of benefit for gas diffusion and mass transport and have been proved to offer more active sites for chemical reaction.[10−12] Since the discovery of mesoporous silica MCM-41 in 1992 by Kresge et al.,[13] ordered mesoporous materials with uniform pore size, tunable pore structure, and high surface area open a new material horizon and occupy an important science position.[14,15] It is evident that mesoporous structure can dramatically increase the surface area and surface-to-volume ratio, which results the improving reaction efficiency and enhanced properties in surface-related applications.[16,17] Beyond the most-investigated silica- or carbon-based materials, ordered mesoporous metal oxides have been extensively investigated due to their more diverse electronic functionality, which includes catalytic activities, semiconductor characteristics, magnetic properties, solar cell applications, and gas-sensing performances.[18−20]

Received: October 11, 2013
Accepted: December 5, 2013
Published: December 5, 2013

  

Mesoporous metal oxides can be directly synthesized by the cooperative assembly of inorganic metal precursors and organic surfactants, also called soft-template method via a sol−gel process.[21−23] Meanwhile, non-template synthetic methods have also been reported to prepare mesoporous metal oxides, such as $Fe_2O_3$, ZnO, and $Co_3O_4$, etc.[24−26] However, the above methods have been limited because of the poor mesoscale phase separation during the framework crystallization, which leads to loss of mesostructured definition. Nanocasting, also called hard-template method, is an efficient approach for synthesis of highly ordered crystalline mesoporous metal oxides, because the hard templates (usually mesoporous silica or carbon) provide stable supports for high-temperature crystallization.[27,28] A large number of mesoporous metal oxides ($Fe_2O_3$, $Cr_2O_3$, $In_2O_3$, $CeO_2$, $Co_3O_4$, NiO, $MoO_2$, $Mn_3O_4$, etc.) have been successfully prepared using the nanocasting method.[29−31] During the conversion of metal precursors in template channel to metal oxides, the inevitable presence of volume shrinkage results the formation of mesoporous metal oxides with low mesostructured ordering and small particle size.[32,33] Recently, we reported an effective container effect in the nanocasting synthesis of mesoporous metal oxides.[34] The size and shape of the container body in conjunction with simply modifying the container opening accessibility can be used to control the escape rate of water and other gas-phase byproducts in the calcination process, and subsequently affect the nanocrystal growth of the materials inside the mesopore space of the template.[34] By utilizing this effect, the mesostructured ordering and particle size of the mesoporous metal oxides, including $Fe_2O_3$, $Cr_2O_3$, $In_2O_3$, $CeO_2$, $Co_3O_4$, NiO, and $Mn_3O_4$ can be controlled in a large range. It is knowledge that the microstructure of the ordered mesoporous metal oxides plays an important role in their application performance. The container effect during nanocasting procedure provides an effective way to research the effect mechanism of mesostructured ordering and particle size of mesoporous metal oxides on their corresponding application property.

Indium oxide ($In_2O_3$), as an n-type and wide band-gap semiconductor (~3.7 eV), is of great interest for use in industrial and technological applications, for example, $In_2O_3$ is widely used for the toxic/dangerous gas detection with particular sensitivity to reducing gases, such as ethanol and ammonia, and oxidizing gases, such as $O_3$.[4] However, $In_2O_3$-based resistive gas sensors possess several critical limitations, such as a limited maximum sensitivity, slow response time and high detection limit. To overcome these fundamental limitations, metal oxide sensing materials including $In_2O_3$ can be opportunely prepared in nanostructured forms, such as nanorods, nanowires, hollow and porous structures, because materials with high surface areas are advantageous for obtaining a good sensing performance.[9,35−38] Among them, ordered mesoporous $In_2O_3$ is believed to be one of the most promising structures because it is with higher surface-to-volume ratio, and moreover, it does not aggregate as easily as nanoscale materials. Tiemann's group reported the improved response of ordered mesoporous $In_2O_3$ to $CH_4$ synthesized using nanocasting method with controlled pore sizes and pore wall thickness.[33] Lai et al. reported the synthesis of ordered mesoporous $In_2O_3$ with enhanced sensitivity to HCHO and studied the influence of pore interconnectivity and size of template.[39] Pellicer's group researched the sensing properties and functional mechanism of CaO-loaded mesoporous $In_2O_3$ to sensing of $CO_2$.[40] However, because of the reasons mentioned above, the effect of mesostructured ordering and particle size of mesoporous $In_2O_3$ on their gas-sensing properties is seldom reported. Thus, there are still great demands for the synthesis of alternative mesoporous $In_2O_3$ with optimum mesostructure and particle size, and further exploiting their novel sensing properties.

In this work, to extend the mesostructured ordering of mesoporous metal oxides and to deepen the comprehension of mesoporous control behaviors for their related applications, $In_2O_3$ acts as a model compound to study the gas sensing properties based on its different mesostructures. The mesostructured ordering and particle size were controlled in a large range using the nanocasting method in conjunction with the container effect during the calcination process. Ethanol gas sensing capability at lower operation temperature by ordered mesoporous $In_2O_3$ with appropriate mesostructured morphology is characteristic for its high sensitivity, improved selectivity, fast response, low detection limit, and good reproducibility. A possible enhancement gas responding mechanism of the $In_2O_3$ sensor was also proposed based on their structure, morphology, and gas-sensing properties.

## EXPERIMENTAL SECTION

**Preparation of Ordered Mesoporous Silica KIT-6.** The mesoporous silica template KIT-6 with *Ia3d* symmetry was prepared according to the procedure described by Ryoo and coworkers.[41] Typically, 6 g of P-123 block copolymer (Sigma) was dissolved in a mixture of 217 mL of deionized water and 10 mL of hydrochloric acid (36%) at 35 °C. Six grams of n-butanol was then added and stirred for 2 h. After the addition of 14 mL of tetraethylorthosilicate (TEOS, 98%), the mixture was stirred at 35 °C for another 24 h. The resulting gel was transferred to a Teflon-lined autoclave and kept for 24 h at 110 °C. The obtained solid sample was filtered off, washed with deionized water, and dried at 60 °C. Finally, the removal of P-123 block copolymer was accomplished by calcination at 550 °C for 6 h under an air atmosphere (heating rate of 2 °C $min^{-1}$).

**Preparation of Mesoporous $In_2O_3$ with Varied Mesostructured Ordering and Particle Size.** Synthesis of ordered mesoporous $In_2O_3$ using KIT-6 as hard template was performed according to the method reported previously by Tian and Yang et al.[30,42] The mesostructured ordering and particle sizes of mesoporous $In_2O_3$ were controlled by utilizing the container effect during the nanocasting procedure, which has been reported in our previous work.[34,43] Typically, indium nitrate pentahydrate ($In(NO_3)_5{\cdot}5H_2O$, 1.0 g) was dissolved in ethanol (10.0 mL) and stirred with KIT-6 (0.5 g) for 1 h. The ethanol was then evaporated off at 40 °C in air. During the evaporation process, the indium precursor was drawn into the pores by capillary action. The mixture of KIT-6 and indium precursor was then thermally decomposed at 400 °C in air for 3 h with a heating rate of 3 °C $min^{-1}$ from room temperature. To obtain ordered mesoporous $In_2O_3$ with varied mesostructured ordering and particle size, the container effect of the thermal treatment can be performed with different container opening accessibility and shape (shown in Figure S1 in the Supporting Information). $In_2O_3$ samples 1, 2, and 3 were respectively obtained by calcination with varied container conditions (covered with glass strips with 100%, 50% coverage, and only placed in the Petri dish). The silica template KIT-6 was then removed by dissolving the preformed $In_2O_3$/KIT-6 composite with hot 2 M NaOH solution twice. The remaining $In_2O_3$ powder was washed several times with water, and then dried at 60 °C in air.

**Characterization.** The wide-angle X-ray powder diffraction (XRD) patterns were recorded at room temperature on a Philips X'pert powder Diffractometer with a graphite monochromator and Fe K$\alpha$1 source ($\lambda$ = 0.193 nm). Typically, the data were collected from 20 to 80°. The average crystallite size was estimated using the Debye-Scherrer equation, $D = K\lambda/(\beta\cos\theta)$, where $D$ is the average crystal diameter, $\beta$ is the corrected peak width (full width at half-maximum),

$K$ is a constant related the shape of the crystallites ($K$ = 0.94), $\lambda$ is the wavelength of the X-rays employed, and $\theta$ is the diffraction angle. The width of the diffraction peak with the highest intensity was selected for the calculation. The small angle X-ray diffraction (SAXRD) data were taken on a Philips X'pert MPD thin film powder XRD using an Cu K$\alpha$ radiation ($\lambda$ = 0.154 nm). Transmission electron microscopy (TEM), high-resolution TEM (HRTEM), and selected area electron diffraction (SAED) measurements were performed on a FEI T20 microscope. All samples subjected to TEM measurements were ultrasonically dispersed in alcohol and drop-cast onto copper grids. The standard and high-resolution scanning electron microscopy (SEM) images were measured on a FEI XL40 instrument. Nitrogen adsorption and desorption isotherms were measured at 77 K on a Micromeritics TriStar porosimiter apparatus. The samples were outgassed at 180 °C overnight before measurements were made. The surface area was obtained by the Brunauer–Emmett–Teller (BET) method and the pore size distribution was calculated from the adsorption branch of the isotherm using the Barrett–Joyner–Halanda (BJH) method.

**Gas Sensor Fabrication and Measurement.** The gas sensors were fabricated by dip-coating a water paste of mesoporous $In_2O_3$ onto alumina ceramic tube with gold electrodes (shown in Figure S2 in the Supporting Information). A Ni–Cr heating wire was inserted into the tube to form an indirect-heated gas sensor to control the operating temperature through varying the heating current. The corresponding relation between the sensing temperature and the heating current was supplied by the gas-sensing measurement system manufacturer. The paste was prepared by mixing of 50 mg of $In_2O_3$ and 0.5 mL of deionized water. The as-modified electrode was dried under ambient conditions overnight before use. Electrical contacts were made with two platinum wires attached to each gold electrode. The electrical properties of the sensor were measured by a CGS-8 series gas-sensing measurement system (Beijing Elite Tech Co., LTD, China). The relative humidity (RH) was about 40%. The gas-sensing properties of the gas sensors were measured under a steady-state condition in an organic glass chamber with a volume of 20 L. An appropriate amount of gas vapor was injected into the closed chamber by a microinjector (microliter syringe used with volume of 0.25, 1, and 10 $\mu$L, respectively) to form the prospective gas concentration of 50 ppb, 200 ppb, 1 ppm, 5 ppm, 20 ppm, 50 ppm, and 100 ppm. And the sensor was exposed to air again by opening the chamber when the test was completed. In order to avoid the disturbing of the testing gas adsorbed on the inner surface of the testing container for the next gas concentration testing, the glass chamber was blown by a blower every time when the container was opened to air in the consecutive concentration testing. The response (sensitivity, $S = R_a/R_g$) of the sensor was defined as the ratio of sensor resistance in dry air ($R_a$) to that in a target gas ($R_g$). The response and recovery times were defined as the times required for a change in the resistance to reach 90% of the equilibrium value after the detected gas was injected and removed, respectively. Ethanol, acetone, methanol, and formaldehyde were used as the detecting gas.

## RESULTS AND DISCUSSION

In previous work, the sensitivity of mesoporous $In_2O_3$ synthesized using nanocasting method was shown to be correlated with the pore size, specific surface area, pore wall thickness, and pore interconnectivity from different replication templates.[33,39] Hence, in this work, in order to avoid the above template effect, a KIT-6 synthesized using an exclusive procedure and exhibiting only pore size, specific surface area, pore wall thickness and pore interconnectivity was used as the hard template. The TEM, SEM, $N_2$ physisorption analysis, and SAXRD of the KIT-6 template are shown in Figure S3 in the Supporting Information and Figure 1b. The TEM image and SAXRD pattern reveal that the KIT-6 template consists uniquely of large ordered mesoporous domains of pure bicontinuous mesostructure with cubic $Ia3d$ symmetry. The mesostructured ordering and particle size of the KIT-6

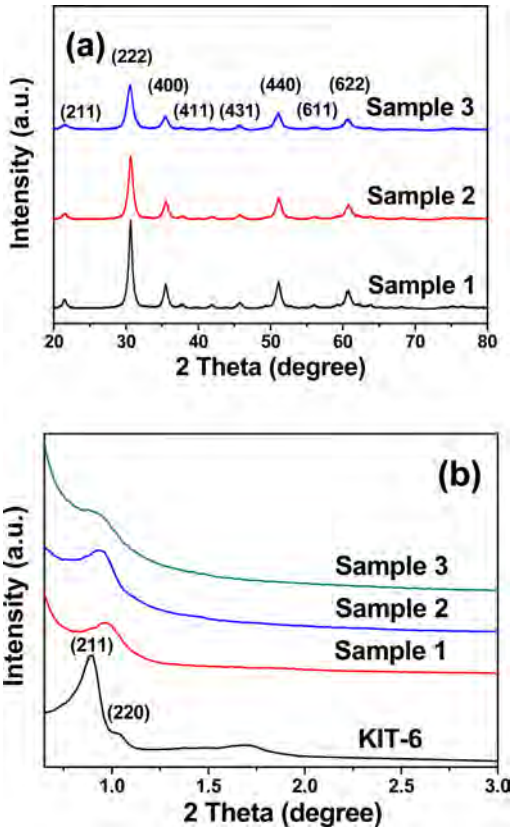


**Figure 1.** (a) XRD patterns of $In_2O_3$ sample 1, 2, and 3; (b) SAXRD patterns of KIT-6, $In_2O_3$ sample 1, 2, and 3.

template is as large as several micrometers from the SEM image. The $N_2$ adsorption–desorption is a type IV and H1 hysteresis loop, indicative of large pores in a narrow range of size. The template has a BET surface area of 692.8 $m^2$ $g^{-1}$, high pore volume reaching 1.2 $cm^3$ $g^{-1}$ and average pore size of 5.4 nm.

Container conditions during the thermal treatment have been proved to have great effect in the mesostruture ordering and particle size during the nanocasting synthesis of mesoporous metal oxides.[34] In this paper, the research aim was to find the particular relation between the mesostructured ordering and particle size of mesoporous $In_2O_3$ and their gas-sensing performance. For this purpose, three distinct container conditions with different container opening accessibility and shape (see Figure S1 in the Supporting Information) during thermal treatment were used to synthesize the ordered mesoporous $In_2O_3$ samples 1, 2, and 3 with controlled mesostructure and particle size. Figure 1a shows the XRD patterns of three $In_2O_3$ samples. Well-defined diffraction peaks indicating the crystalline nature can be indexed well to the body-centered cubic (bcc) phase of bixbyite $In_2O_3$ (JCPDS card No. 06-0416). With the increase in the container opening (from $In_2O_3$ sample 1 to 2 and 3), there is continuous broadening of each XRD pattern peak, attributed to the decrease in crystallite size. By using the Debye–-Scherrer equation for the full-width at half-maximum (fwhm) of the (222) reflection, the average crystallite sizes were calculated to be 19.6, 17.9, and 12.0 nm, respectively. One can see that, with the increase in the container opening, the crystal domain sizes decrease; nevertheless, the average crystallite size of sample 3 (12.0 nm) is still more than the repeat distance of the


dx.doi.org/10.1021/am4044807 | ACS Appl. Mater. Interfaces 2014, 6, 401–409

mesopores. This phenomenon could also be confirmed by the HRTEM image (see Figure S4 in the Supporting Information), which shows that part of one mesoporous particle is crystallized in the same direction and the lattice fringes of the walls are around several small mesopores.[36] In other words, the presence of regular arranged mesopores do not seem to disturb the atomic-scale crystallinity of $In_2O_3$. This is different from many other mesoporous metal oxides which have been synthesized by structure replication (e.g., ZnO,[44] MgO,[45] $CeO_2$[33]), where the single-crystalline grains turned out to be hardly larger than the pore wall thickness. The SAXRD patterns of three $In_2O_3$ samples show one intense peak at $2\theta$ of around 0.95°, corresponding to the 211 diffraction peak of *Ia*3*d* symmetry, which indicates that the long-range mesostructured regularity of KIT-6 is well-retained in all $In_2O_3$ replicas. Comparing to the SAXRD pattern of KIT-6, the disappearance of the shoulder peak at $2\theta$ = 1.08° indicates that the mesoporous structure of $In_2O_3$ is lower than that of KIT-6. Meanwhile, with the increase of the container opening, the intensity of the 211 diffraction peak decreases, which can be interpreted as a reduction in the X-ray scattering contrast between the pore and the framework,[39] revealing that the mesostructured ordering of $In_2O_3$ can be varied by the change of the container conditions.

The container effect for the synthesis of $In_2O_3$ with varied mesostructured ordering and particle size can be clearly observed from the SEM images shown in Figure 2. All $In_2O_3$

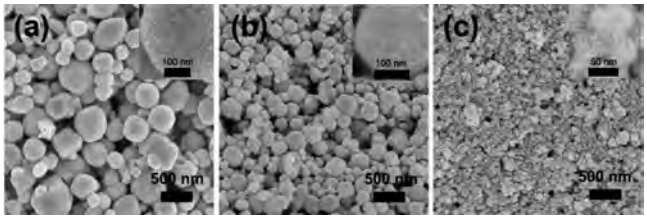


**Figure 2.** SEM and high-resolution SEM images (insets) of $In_2O_3$ samples (a) 1, (b) 2, and (c) 3.

samples exhibit nearly spherical particles. The morphology is totally different from their parent template KIT-6, which is irregular in shape and much larger than the $In_2O_3$ replica (shown in Figure S3b in the Supporting Information). The average particle size of the $In_2O_3$ samples decreases (from 369.5 nm to 258.6 nm and 44.8 nm) with the increase of the container opening. These values were obtained by measuring the size of about 80 particles for each sample. From the high-resolution SEM images inserted in Figure 2, one can see that the whole $In_2O_3$ particle is highly ordered with regular mesopores, which means that the size of the mesostructured ordering is equal with the particle diameter. Obviously, the mesostructured ordering and particle sizes of the $In_2O_3$ samples can be controlled easily and in a large range by the "container effect". The TEM images shown in Figure 3 reveal that all the $In_2O_3$ samples have sphere-like morphology with periodic cubic (*Ia*3*d*) mesostructure. The particle sizes and mesostructured ordering markedly decreased with the increase of the container opening, which is in good agreement with the SAXRD and SEM results. For $In_2O_3$ sample 3, one can see the presence of many isolated nanoparticles with diameter less than 10 nm and without any long-range mesoporous periodicity, which arises from the "solid decomposition" of metal precursor during the thermal treatment procedure for open system nanocasting synthesis.[34] The SAED data for three samples (inserted in

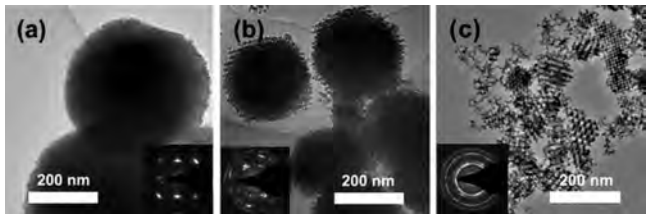


**Figure 3.** TEM images and SAED patterns (inserted) of $In_2O_3$ samples (a) 1, (b) 2, and (c) 3.

Figure 3) are with different patterns (sample 1 with only spots, sample 2 with spots and rings, sample 3 with only rings), which indicates that the crystallinity and crystallite sizes decreases with the container opening, corresponding to the XRD results.

The $N_2$ physisorption results of three $In_2O_3$ samples are shown in Figure 4. All $In_2O_3$ samples gave a typical IV isotherm

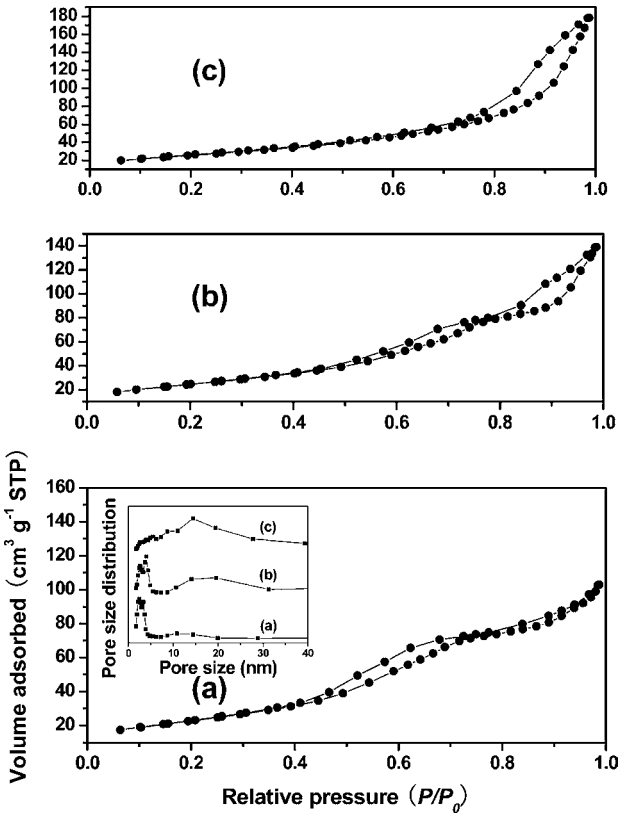


**Figure 4.** Nitrogen physisorption isotherms and pore size distributions (inset) of $In_2O_3$ samples (a) 1, (b) 2, and (c) 3 (pore size distributions are shifted for clarity).

with a clear H1-type hysteresis loop, which is characteristic for mesoporous materials. Clearly, with the increase of the container opening, the hysteresis loops occur at much higher relative pressures, indicating much larger mesoporous diameters, a fact also substantiated by the pore size distributions calculated by the BJH method (inserted in Figure 4a).[39] The average pore size of sample 3 with only one large hysteresis loop ($P/P_o$ = 0.4−1.0) is 14.4 nm, which arises from the piled porosity by the aggregation of nanoparticles. Whereas for sample 1 and sample 2, two well-defined steps of capillary condensation corresponding to two pore size distributions (2.4 and 10.8 nm for sample 1, 3.9, and 17.5 nm for sample 2) can be observed. The former pore is caused by the replica from the


dx.doi.org/10.1021/am4044807 | ACS Appl. Mater. Interfaces 2014, 6, 401−409

KIT-6 template, and a narrow pore size distribution confirms the highly ordered uniform pore structure. The latter with large pore size distribution comes from the aggregation of mesoporous particles. The specific surface areas of all $In_2O_3$ samples are 84, 90, and 91 $m^2\ g^{-1}$, respectively. All the above data are lower than that of the parent KIT-6 template, which has been observed by previous work and may be mainly attributed to the lower structural order and larger density.[33,43]

As discussed above, for nanocasting synthesis, the container conditions have a significant effect on the mesostructured ordering, particle size, crystallinity, and even pore size distribution of the mesoporous $In_2O_3$. It can be ascribed to the container influence on the escape rate of water and nitrogen oxide byproducts, which in turn affects the diffusion rates of precursor and the structure of final product (see Figure S5 in the Supporting Information). During calcination, the entire container is saturated with water vapor, which comes from the precursor solution and reduces of the water content of the precursor. Hence, the container opening and shapes can be utilized to tune the residual water amount within the inner pore space of the template, and thus be used to control the transportation rate of the indium precursor in liquid or solid phase and obtain the final mesoporous $In_2O_3$ with controlled structure and morphology.[34]

Given the fact that the operation temperature of semiconducting gas sensor devices ranges from room temperature to several hundred degrees Celsius, it is mandatory that mesoporous metal oxides for gas-sensing application are temperature-stable and can withstand these thermal conditions without substantial loss in porosity. Nanocasting is an efficient approach for the synthesis of ordered mesoporous metal oxides with high thermal stability, because the hard template provides stable and rigid supports for high-temperature crystallization. In order to investigate the heat resistance, we placed $In_2O_3$ sample 2 in a Muffle furnace and calcinated it at 600 and 700 °C. SAXRD patterns, $N_2$ physisorption analysis, and TEM images of sample 2 before and after the thermal treatment are shown in Figure 5. The physisorption isotherm shape and pore size distribution, more importantly, the SAXRD pattern of $In_2O_3$ calcinated at 600 °C remain mostly the same with the as-prepared $In_2O_3$ sample, which confirms that no significant loss in mesostructured regularity or porosity takes place. The specific surface area and pore volume decreases only by 32% (from 90 to 61 $m^2\ g^{-1}$) and 4.8% (from 0.21 to 0.20 $cm^3\ g^{-1}$). At 700 °C, the 211 diffraction peak of SAXRD pattern disappears, whereas the specific surface area is still as high as 42 $m^2\ g^{-1}$ with pore volume of 0.17 $cm^3\ g^{-1}$. The average pore size shifts to one distribution of 8.6 nm, which indicates that most of the replica mesopores loss and the piled mesopores get smaller because of the crystalline growth at high temperature. These results are also confirmed by the TEM contrast images (Figure 5c, d), which reveals that mesoporous $In_2O_3$ samples synthesized by the container effect nanocasting method are good candidates for high temperature gas-sensing application.

It is known that the structure and morphology of functional materials have a large effect on their physical, chemical and application properties. For example, the sensing performance of metal oxide sensors (e.g., $Fe_2O_3$, ZnO, $In_2O_3$) have been reported to vary a lot with the different porous morphology.[39,46,47] In this work, the container effect was used to control the mesostructured ordering and particle size of mesoporous $In_2O_3$. It is expected that such a morphology controlling method might bring about more efficient gas sensing as

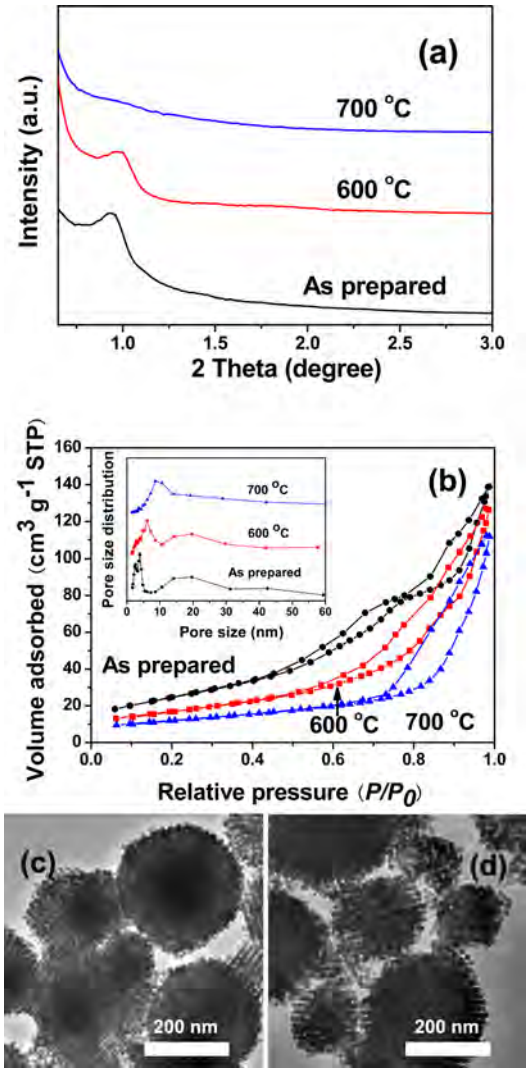


**Figure 5.** (a) SAXRD patterns, (b) nitrogen physisorption isotherms (inset, pore size distributions), and (c, d) TEM images ((c) 600 and (d) 700 °C) of $In_2O_3$ sample 2 before (as-prepared) and after thermal treatment at 600 and 700 °C (pore size distributions are shifted for clarity).

compared to conventionally prepared mesoporous $In_2O_3$ with unique structure. Figure S2 in the Supporting Information shows the component of the as-prepared $In_2O_3$ sensor. At first, the temperature-dependence behavior and the optimum operating temperature of the as-prepared three $In_2O_3$ sensors to 50 ppm of ethanol was investigated through varying the heating current to achieve the highest sensitivity (Figure 6a). Bulk $In_2O_3$ particles used as a benchmark were found to be the least sensitive to the presence of ethanol with the optimum operating temperature of 300 °C. In contrast, the as-prepared three $In_2O_3$ sensors exhibited a much better response at the range of operating temperature. The optimum operating temperatures of three $In_2O_3$ samples were 240, 220, and 270 °C with sensitivity of 26.8, 31.2, and 21.3, respectively. One can see that the sensitivity of the sensors presents a trend of "increase-maximum-decay" with an increase in temperature. As the temperature increases, a higher response is observed because of the activation of adsorbed molecular oxygen and lattice oxygen to form active $O_2^-$ and $O^-$ and mobile $O^{2-}$ species, respectively.[9] This phenomenon continues up to a


dx.doi.org/10.1021/am4044807 | ACS Appl. Mater. Interfaces 2014, 6, 401−409

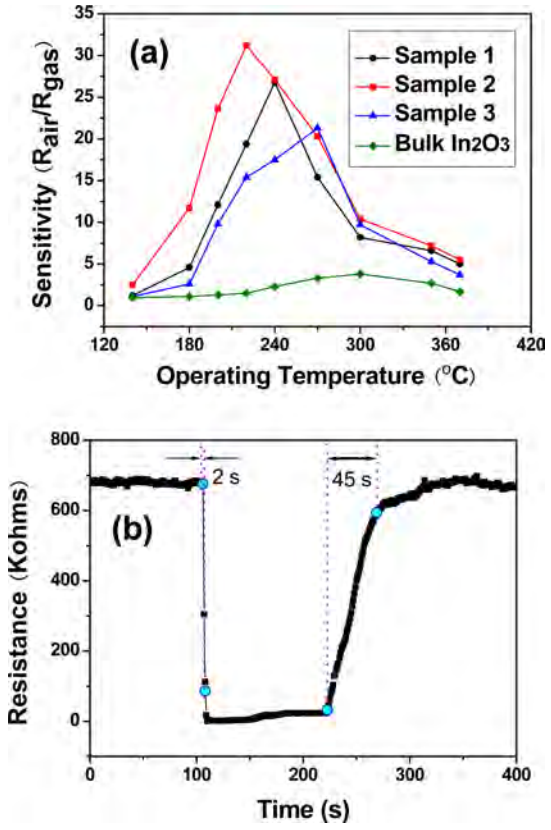


**Figure 6.** (a) Sensitivity versus operating temperature of $In_2O_3$ samples exposed to 50 ppm of ethanol; (b) dynamic ethanol sensing transient of $In_2O_3$ sample 2 to 50 ppm of ethanol at 220 °C.

certain optimum temperature, beyond which exothermic gas adsorption becomes difficult and gas molecules begin to desorb in large quantities, leading to a drop in sensor response.[37] Thus, the optimum temperature is a balance point between two conflicting mechanisms. It can be seen that the mesoporous morphology influenced the gas sensing properties significantly. $In_2O_3$ sample 2 displayed the largest response value (31.2) at the lowest optimal temperature of 220 °C. This may be attributed to the different structure and morphology of the as-prepared $In_2O_3$ materials, including the specific surface area, particle size, and porosity, which greatly affect the adsorption, diffusion, and desorption of gas molecules and finally influence the oxygen state, base resistance, gas reactivity and optimum operating temperature of the materials.[35] A detail underlying reasons for the observed behavior still need further study and will be discussed later. Thus, we choose 220 °C as our working temperature to proceed with the subsequent detections.

The response and recovery times are also important parameters for a gas sensor, which were defined as the time to reach 90% of the final equilibrium value after the detected gas was injected and removed, respectively. The response and recovery times of $In_2O_3$ sample 2 shown in Figure 6b to 50 ppm of ethanol are 2 s and 45 s, respectively, while that to 100 ppm of ethanol are 1 s and 76 s, respectively. The gas response of various $In_2O_3$ nanostructures to 100 ppm of ethanol in previous literatures and present study are summarized in Table 1. The ethanol response time of $In_2O_3$ sample 2 is among the fastest values, whereas the recovery times for three $In_2O_3$ samples in our work are longer than most of the reported $In_2O_3$ sensors, which was also observed in the nanoporous $In_2O_3$ hollow spheres sensor with short response time and long recovery time.[48]

It is knowledge that the development of gas sensor that can sense gas at lower detection concentration and allow quantification of gas over a wide concentration range is of practical interest. Figure 7a–c show the representative dynamic responses as a function of ethanol concentration for three $In_2O_3$ samples with varied mesoporous structures. It was obvious that all the $In_2O_3$-based sensors had a wide detection range for ethanol from 50 ppb to 100 ppm. The response values to 50 ppb of ethanol for three $In_2O_3$ samples are all larger than 1.2. To the best of our knowledge, this is the lowest concentration that had been reported for nanostructured $In_2O_3$ sensors to ethanol. With the increasing of the ethanol concentration, the responses greatly increase. The sensor sensitivities of these three samples as a function of ethanol concentration are provided in Figure 7d. It can be seen that $In_2O_3$ sample 2 is much more sensitive than the other $In_2O_3$ samples. Taking 100 ppm as an example, $In_2O_3$ sample 2 exhibits a sensitivity of 63.4, which is more than twice higher than that (27.9) of $In_2O_3$ sample 3. That means the sensitivity of mesoporous $In_2O_3$ could be controlled by adjusting the mesostructured ordering and particle size. It should also be pointed out that $In_2O_3$ sample 2 also possesses superior performance when compared with other nanostructured $In_2O_3$ sensors reported in previous works (shown in Table 1), which means that container effect is an effective method to synthesize high sensitivity mesoporous $In_2O_3$ sensor.

Figure 8a illustrates the response of three $In_2O_3$ samples to 50 ppm of various gases, including $C_2H_5OH$, $C_3H_6O$, $CH_3OH$, and HCHO at the operating temperature of 220 °C. Obviously,

**Table 1. Gas-Sensing Properties of Various $In_2O_3$ Nanostructures to 100 ppm of Ethanol in the Literature and Present Study**

| sensing $In_2O_3$ materials | operating temperature (°C) | sensor response | response time (s) | recovery time (s) | detection limit (ppm) | ref |
|---|---|---|---|---|---|---|
| $In_2O_3$ sample 1 | 220 | 39.2 | 56 | 113 | 0.05 | present study |
| $In_2O_3$ sample 2 | 220 | 63.4 | 1 | 76 | 0.05 | present study |
| $In_2O_3$ sample 3 | 220 | 27.9 | 74 | 119 | 0.05 | present study |
| $In_2O_3$:Er hollow spheres | 215 | 40.3 | 10 | 23 | 7 | 55 |
| hierarchical $In_2O_3$ nanotubes | | 15.0 | 7 | 9 | 5 | 52 |
| $In_2O_3$:Ta particles | 500 | 16.9 | | | 10 | 56 |
| Porous $In_2O_3$ nanowires | 260 | 62.6 | 5 | 7 | 2 | 57 |
| ZnO-$In_2O_3$ nanofibers | 210 | 25.0 | 2 | 1 | 1 | 58 |
| Co-doped $In_2O_3$ nanowires | 300 | 17.0 | 2 | 3 | 5 | 59 |
| nanoporous $In_2O_3$ hollow spheres | 400 | 137.2 | 2 | 830 | 20 | 48 |
| $In_2O_3$ porous nanoparticles | 200 | 4.0 | 6 | 15 | 100 | 60 |


dx.doi.org/10.1021/am4044807 | ACS Appl. Mater. Interfaces 2014, 6, 401–409

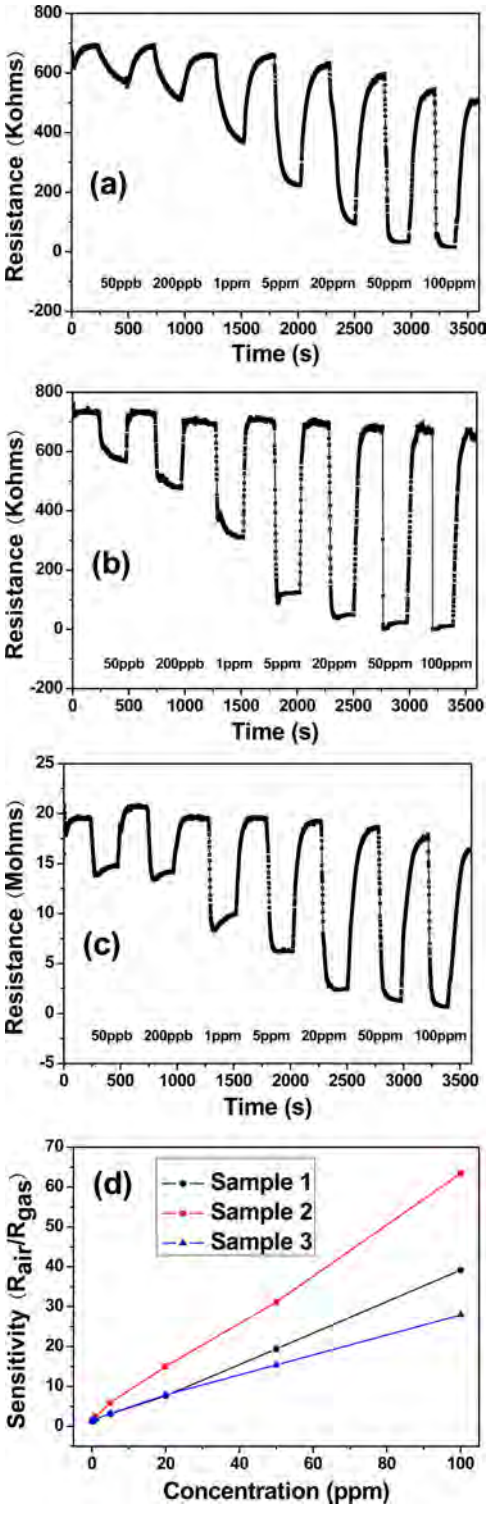


**Figure 7.** Typical response and recovery curves to different ethanol concentration of $In_2O_3$ samples (a) 1, (b) 2, and (c) 3; (d) sensor sensitivity of three $In_2O_3$ samples with varied ethanol concentration.

the responses of $In_2O_3$ sample 2 to four gases are all improved compared with the other ones, and the largest increase is observed for ethanol, implying the good selective detection of the sample 2 sensor to ethanol. High sensor responses of 31.2, 14.5, 12.5, and 13.2 were obtained from the mesoporous $In_2O_3$ sample 2 for 50 ppm of ethanol, acetone, methanol and formaldehyde, respectively, which are 2-5 times higher than that

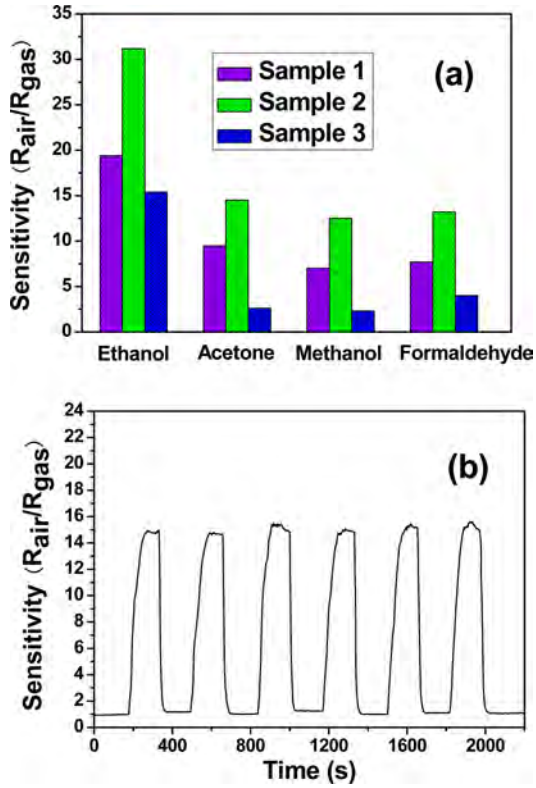


**Figure 8.** (a) Sensitivity values of three $In_2O_3$ samples to 50 ppm of various gases: ethanol, acetone, methanol, and formaldehyde; (b) sensitivity reproducibility of the $In_2O_3$ sample 2 to 20 ppm of ethanol at 220 °C.

for $In_2O_3$ sample 3. These results strongly prove that the mesoporous morphology of $In_2O_3$, including the mesostructured ordering and particle size, have great effect on their gas-sensing properties. Stability, that is, the ability to retain performance characteristics over time, is another important characteristic of gas sensor. In order to study the stability of $In_2O_3$ sample 2, the as-prepared sensor was operated upon six successive sensing tests to 20 ppm of ethanol. Figure 8b exhibits the reproducibility of the $In_2O_3$ sample 2, revealing that the sensor maintains its initial response without a clear decrease and have a satisfying long-term stability and reproducibility.

As generally mentioned, the gas-sensing mechanism of $In_2O_3$-based sensors belongs to the "redox" process, which is based on the change in resistance that is mainly caused by the adsorption and desorption of gas molecules on the sensor surface.[49,50] Stoichiometric $In_2O_3$ is firstly transformed into nonstoichiometric $In_2O_{3-x}$ during calcination at high temperature, which results an n-type semiconductor with deficiency of oxygen. Once exposed to air, oxygen molecules are adsorbed on the surface and form $O_2^-$, $O^{2-}$, and $O^-$ ions through trapping the electrons from the conductance band of $In_2O_{3-x}$. Thus, the resistance of the sensor increases. If the sensor is exposed to reducing gases, such as ethanol, they may react with the absorbed oxygen molecules and release electrons to the $In_2O_3$ surface. As a result, the resistance of the sensor is eventually decreased.

From the above results, $In_2O_3$ sample 2 has the highest gas response, whereas $In_2O_3$ samples 1 and 3 have the lower one. The obvious difference of gas-sensing properties between three $In_2O_3$ samples confirms that container effect is an efficient nanocasting method to optimize the gas sensitivity of


dx.doi.org/10.1021/am4044807 | ACS Appl. Mater. Interfaces 2014, 6, 401−409

mesoporous $In_2O_3$ materials by controlling the mesostructured ordering and particle size. In general, the gas-sensing performance of metal oxides depends on several factors, such as surface areas, particle sizes, and porous structures, which greatly affect the adsorption and diffusion of gas molecules and carriers mobility.[51,52] The BET specific surface areas of $In_2O_3$ sample 2 (90 $m^2$ $g^{-1}$) and 3 (91 $m^2$ $g^{-1}$) are a little higher than that of $In_2O_3$ sample 1 (84 $m^2$ $g^{-1}$), which should be beneficial for their gas-sensing. However, because the difference of the BET specific surface areas for three $In_2O_3$ samples may be negligible, the main factors to influence the $In_2O_3$ gas-sensing properties should be related to the other reasons, such as particle sizes and porous structures. In our case, since the pore size, pore wall thickness and pore interconnectivity of $In_2O_3$ are very similar because of using the same KIT-6 replication template, the effective electron depletion area should arise from the effective diffusion of target gases within the sensing lay. The average particle sizes of three $In_2O_3$ samples are 369.5, 258.6, and 44.8 nm, respectively. $In_2O_3$ samples 1 and 2 are with ordered mesoporous sphere morphology, whereas sample 3 is composed of less ordered mesostructured nanoparticles. During the high-temperature thermal treatment and operation of the sensor device, sample 3 suffers from grain growth easily and forms more compact nanoparticle aggregation, while sample 1 and 2 are more stable and prefer to maintain their mesoporous structures. This phenomenon has been proved by the BJH average pore size distributions (inset in Figure 4a), in which only larger piled pores can be observed for sample 3 without the ordered replica pores. Lai and co-workers and Wang et al. separately reported that particle size and morphology of metal oxide materials had great influence on their thickness of electron depletion layer and diffusion of gas molecules during the gas sensing.[39,53] In our case (Figure 9),

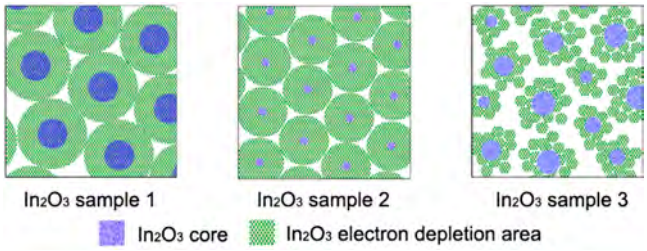


**Figure 9.** Illustration of respective sensing factors of three $In_2O_3$ samples.

for compact nanoparticle sample 3, it is theoretically difficult for target gas to diffuse into the interior of the sensing layer and only small electron depletion area can form. Therefore, poor gas response is expectable, even though its BET area is the highest among three samples. Sample 1 and 2 are with the similar mesoporous morphology except for their mesostructure ordering and particle size. Tiemann et al. indicated that Knudsen diffusion is the main diffusion type for metal oxide gas-sensing materials with smaller pores sizes (several nanometers) and bigger pores are favorable for the diffusion of gas molecules.[54] Sample 1 with larger particle size and more ordered mesostructures decreases the proportion of larger piled pores (inset in Fig 4a), makes the diffusion of target gases within the sensing layer comparably hard, and results the short effective diffusion distance and small electron depletion area, which leads to the lower gas-sensing performance, compared with that of sample 2. For sample 2, large surface area with enough sensing active sites, proper diffusion channel of small intraparticle mesopores and big interparticle mesopores, and appropriate particle size for effective electron depletion are all causes for the best sensor response. These results indicate that the "container effect" nanocasting way is an effective method to synthesize the optimal mesoporous $In_2O_3$ materials with promising gas-sensing performance.

## CONCLUSIONS

In summary, mesoporous $In_2O_3$ with controlled mesostructured ordering and particle size were fabricated using a facile nanocasting technique together with a container effect method. The gas-sensing properties of the $In_2O_3$ samples were studied in detail and the mesostructured morphology could be used to modify the gas-sensing properties significantly, including an improved response, a decreased detection limit and a shortened response dynamics. The synthesized mesoporous $In_2O_3$ with the optimal mesostructures showed the highest sensitivity to ethanol because of its large surface area, proper pore distribution, and appropriate particle size, which supply enough sensing active sites, sufficient gas diffusion, and effective electron depletion. The present result evidently proves that the mesostrucuture ordering control strategy by nanocasting container effect method would be one of the most promising guides for advanced mesoporous-based metal oxide gas sensors.

## ASSOCIATED CONTENT

### Supporting Information

Different container opening accessibility and shape for preparation of $In_2O_3$ samples 1, 2, and 3, scheme of $In_2O_3$ gas sensor, TEM, SEM, $N_2$ physisorption isotherm and pore size distribution of the KIT-6 template, HRTEM image of $In_2O_3$ sample 2, container effect mechanism in the nanocasting synthesis of mesoporous $In_2O_3$. This material is available free of charge via the Internet at http://pubs.acs.org.

## AUTHOR INFORMATION

### Corresponding Authors

*E-mail: sunxh@tju.edu.cn.
*E-mail: zhengchunming@tjpu.edu.cn.

### Notes

The authors declare no competing financial interest.

## ACKNOWLEDGMENTS

This work was supported by funding from the National Natural Science Foundation of China, NSFC (51172157, 51202159, 51208357, 51372166), Fund for the Doctoral Program of Higher Education, Ministry of Education of China (20120032120017), General Program of Municipal Natural Science Foundation of Tianjin (13JCYBJC16900, 13JCQNJC08200), Beiyang Scholar Plan for Excellent Young Teachers of Tianjin University and Key Program of Municipal Natural Science Foundation of Tianjin (12JCZDJC27500).

## REFERENCES

(1) Zaera, F. *Chem. Soc. Rev.* **2013**, *42*, 2746−2762.
(2) Jiang, J. A.; Li, Y. Y.; Liu, J. P.; Huang, X. T. *Nanoscale* **2011**, *3*, 45−58.
(3) Chandra, S.; Barick, K. C.; Bahadur, D. *Adv. Drug Delivery Rev.* **2011**, *63*, 1267−1281.
(4) Arafat, M. M.; Dinan, B.; Akbar, S. A.; Haseeb, A. *Sensors* **2012**, *12*, 7207−7258.

(5) Giordano, L.; Pacchioni, G. *Accounts Chem. Res.* **2011**, *44*, 1244−1252.
(6) Shi, J. L. *Chem. Rev.* **2013**, *113*, 2139−2181.
(7) Devan, R. S.; Patil, R. A.; Lin, J. H.; Ma, Y. R. *Adv. Funct. Mater.* **2012**, *22*, 3326−3370.
(8) Zhou, K. B.; Li, Y. D. *Angew. Chem., Int. Ed.* **2012**, *51*, 602−613.
(9) Sun, Y. F.; Liu, S. B.; Meng, F. L.; Liu, J. Y.; Jin, Z.; Kong, L. T.; Liu, J. H. *Sensors* **2012**, *12*, 2610−2631.
(10) Larcher, D.; Masquelier, C.; Bonnin, D.; Chabre, Y.; Masson, V.; Leriche, J. B.; Tarascon, J. M. *J. Electrochem. Soc.* **2003**, *150*, A133−A139.
(11) Debecker, D. P.; Hulea, V.; Mutin, P. H. *Appl. Catal. A* **2013**, *451*, 192−206.
(12) Sun, B.; Horvat, J.; Kim, H. S.; Kim, W. S.; Ahn, J.; Wang, G. X. *J. Phys. Chem. C* **2010**, *114*, 18753−18761.
(13) Kresge, C. T.; Leonowicz, M. E.; Roth, W. J.; Vartuli, J. C.; Beck, J. S. *Nature* **1992**, *359*, 710−712.
(14) Davis, M. E. *Nature* **2002**, *417*, 813−821.
(15) Hartmann, M. *Chem. Mater.* **2005**, *17*, 4577−4593.
(16) Sayari, A.; Hamoudi, S. *Chem. Mater.* **2001**, *13*, 3151−3168.
(17) Schuth, F.; Schmidt, W. *Adv. Mater.* **2002**, *14*, 629−638.
(18) Schuth, F. *Chem. Mater.* **2001**, *13*, 3184−3195.
(19) Yu, C. Z.; Tian, B. Z.; Zhao, D. Y. *Curr. Opin. Solid State Mater. Sci.* **2003**, *7*, 191−197.
(20) Agarwala, S.; Kevin, M.; Wong, A. S. W.; Peh, C. K. N.; Thavasi, V.; Ho, G. W. *ACS Appl. Mater. Interfaces* **2010**, *2*, 1844−1850.
(21) Yang, P. D.; Zhao, D. Y.; Margolese, D. I.; Chmelka, B. F.; Stucky, G. D. *Nature* **1998**, *396*, 152−155.
(22) Tian, B. Z.; Liu, X. Y.; Tu, B.; Yu, C. Z.; Fan, J.; Wang, L. M.; Xie, S. H.; Stucky, G. D.; Zhao, D. Y. *Nat. Mater.* **2003**, *2*, 159−163.
(23) Fan, J.; Boettcher, S. W.; Stucky, G. D. *Chem. Mater.* **2006**, *18*, 6391−6396.
(24) Cong, H.-P.; Yu, S.-H. *Cryst. Growth Des.* **2009**, *9*, 210−217.
(25) Zhang, J.; Wang, S.; Xu, M.; Wang, Y.; Zhu, B.; Zhang, S.; Huang, W.; Wu, S. *Cryst. Growth Des.* **2009**, *9*, 3532−3537.
(26) Liu, X. H.; Zhang, J.; Guo, X. Z.; Wu, S. H.; Wang, S. R. *Nanotechnology* **2010**, *21*, 095501.
(27) Yang, H. F.; Zhao, D. Y. *J. Mater. Chem.* **2005**, *15*, 1217−1231.
(28) Lu, A. H.; Schuth, F. *Adv. Mater.* **2006**, *18*, 1793−1805.
(29) Jiao, F.; Harrison, A.; Jumas, J. C.; Chadwick, A. V.; Kockelmann, W.; Bruce, P. G. *J. Am. Chem. Soc.* **2006**, *128*, 5468−5474.
(30) Tian, B. Z.; Liu, X. Y.; Yang, H. F.; Xie, S. H.; Yu, C. Z.; Tu, B.; Zhao, D. Y. *Adv. Mater.* **2003**, *15*, 1370−1374.
(31) Shi, Y.; Guo, B.; Corr, S. A.; Shi, Q.; Hu, Y.-S.; Heier, K. R.; Chen, L.; Seshadri, R.; Stucky, G. D. *Nano Lett.* **2009**, *9*, 4215−4220.
(32) Yue, W.; Zhou, W. *Prog. Nat. Sci.* **2008**, *18*, 1329−1338.
(33) Waitz, T.; Wagner, T.; Sauerwald, T.; Kohl, C. D.; Tiemann, M. *Adv. Funct. Mater.* **2009**, *19*, 653−661.
(34) Sun, X. H.; Shi, Y. F.; Zhang, P.; Zheng, C. M.; Zheng, X. Y.; Zhang, F.; Zhang, Y. C.; Guan, N. J.; Zhao, D. Y.; Stucky, G. D. *J. Am. Chem. Soc.* **2011**, *133*, 14542−14545.
(35) Lai, X. Y.; Li, J.; Korgel, B. A.; Dong, Z. H.; Li, Z. M.; Su, F. B.; Du, J.; Wang, D. *Angew. Chem., Int. Ed.* **2011**, *50*, 2738−2741.
(36) Mao, D.; Yao, J. X.; Lai, X. Y.; Yang, M.; Du, J.; Wang, D. *Small* **2011**, *7*, 578−582.
(37) Li, Z. M.; Lai, X. Y.; Wang, H.; Mao, D.; Xing, C. J.; Wang, D. *J. Phys. Chem. C* **2009**, *113*, 2792−2797.
(38) Yu, R.; Li, Z.; Wang, D.; Lai, X.; Xing, C.; Yang, M.; Xing, X. *Scr. Mater.* **2010**, *63*, 155−158.
(39) Lai, X. Y.; Wang, D.; Han, N.; Du, J.; Li, J.; Xing, C. J.; Chen, Y. F.; Li, X. T. *Chem. Mater.* **2010**, *22*, 3033−3042.
(40) Prim, A.; Pellicer, E.; Rossinyol, E.; Peiro, F.; Cornet, A.; Morante, J. R. *Adv. Funct. Mater.* **2007**, *17*, 2957−2963.
(41) Kleitz, F.; Choi, S. H.; Ryoo, R. *Chem. Commun.* **2003**, *17*, 2136−2137.
(42) Yang, H. F.; Shi, Q. H.; Tian, B. Z.; Lu, Q. Y.; Gao, F.; Xie, S. H.; Fan, J.; Yu, C. Z.; Tu, B.; Zhao, D. Y. *J. Am. Chem. Soc.* **2003**, *125*, 4724−4725.
(43) Sun, X. H.; Shi, Y. F.; Ji, H. M.; Li, X. L.; Cai, S.; Zheng, C. M. *J. Alloy. Compd.* **2012**, *545*, 5−11.
(44) Waitz, T.; Tiemann, M.; Klar, P. J.; Sann, J.; Stehr, J.; Meyer, B. K. *Appl. Phys. Lett.* **2007**, *90*, 123108.
(45) Roggenbuck, J.; Tiemann, M. *J. Am. Chem. Soc.* **2005**, *127*, 1096−1097.
(46) Yan, W.; Fan, H. Q.; Zhai, Y. C.; Yang, C.; Ren, P. R.; Huang, L. M. *Sens. Actuator B-Chem.* **2011**, *160*, 1372−1379.
(47) Wagner, A.; Bakin, A.; Otto, T.; Zimmermann, M.; Jahn, B.; Waag, A. *Thin Solid Films* **2012**, *520*, 4662−4665.
(48) Kim, S.-J.; Hwang, I.-S.; Choi, J.-K.; Kang, Y. C.; Lee, J.-H. *Sens. Actuator B* **2011**, *155*, 512−518.
(49) Korotcenkov, G.; Cerneavschi, A.; Brinzari, V.; Vasiliev, A.; Ivanov, M.; Cornet, A.; Morante, J.; Cabot, A.; Arbiol, J. *Sens. Actuator B* **2004**, *99*, 297−303.
(50) Zuruzi, A. S.; MacDonald, N. C.; Moskovits, M.; Kolmakov, A. *Angew. Chem., Int. Ed.* **2007**, *46*, 4298−4301.
(51) Liu, X. J.; Chang, Z.; Luo, L.; Lei, X. D.; Liu, J. F.; Sun, X. M. *J. Mater. Chem.* **2012**, *22*, 7232−7238.
(52) Zai, J. T.; Zhu, J.; Qi, R. R.; Qian, X. F. *J. Mater. Chem. A* **2013**, *1*, 735−745.
(53) Wang, L. L.; Fei, T.; Lou, Z.; Zhang, T. *ACS Appl. Mater. Interfaces* **2011**, *3*, 4689−4694.
(54) Tiemann, M. *Chem.—Eur. J.* **2007**, *13*, 8376−8388.
(55) Zhang, T.; Gu, F. B.; Han, D. M.; Wang, Z. H.; Guo, G. S. *Sens. Actuators, B* **2013**, *177*, 1180−1188.
(56) Bloor, L. G.; Manzi, J.; Binions, R.; Parkin, I. P.; Pugh, D.; Afonja, A.; Blackman, C. S.; Sathasivam, S.; Carmalt, C. J. *Chem. Mater.* **2012**, *24*, 2864−2871.
(57) Liu, J.; Guo, Z. P.; Zhu, K. X.; Wang, W. J.; Zhang, C. F.; Chen, X. L. *J. Mater. Chem.* **2011**, *21*, 11412−11417.
(58) Zhang, X. J.; Qiao, G. J. *Appl. Surf. Sci.* **2012**, *258*, 6643−6647.
(59) Li, Z.; Dzenis, Y. *Talanta* **2011**, *85*, 82−85.
(60) Wang, L.; Tang, F.; Ozawa, K.; Chen, Z.-G.; Mukherj, A.; Zhu, Y.; Zou, J.; Cheng, H.-M.; Lu, G. Q. *Angew. Chem., Int. Ed.* **2009**, *48*, 7048−7051.